

Internal dynamics of the radio–halo cluster A2219: a multi–wavelength analysis [★]

W. Boschin¹, M. Girardi¹, R. Barrena^{2,3}, A. Biviano⁴, L. Feretti⁵, and M. Ramella⁴

¹ Dipartimento di Astronomia, Università degli Studi di Trieste, via Tiepolo 11, 34131 Trieste, Italy
e-mail: boschin, girardi@ts.astro.it

² Instituto de Astrofísica de Canarias, E-38200 La Laguna, Tenerife, Spain
e-mail: rbarrena@ll.iac.es

³ INAF - Telescopio Nazionale Galileo, Roque de Los Muchachos, PO box 565, 38700 Santa Cruz de La Palma, Spain

⁴ INAF - Osservatorio Astronomico di Trieste, via Tiepolo 11, 34131 Trieste, Italy
e-mail: biviano, ramella@ts.astro.it

⁵ Istituto di Radioastronomia del C.N.R., via Gobetti 101, 40129 Bologna, Italy
e-mail: lferetti@ira.cnr.it

Received / Accepted

Abstract. We present the results of the dynamical analysis of the rich, hot, and X–ray very luminous galaxy cluster A2219, containing a powerful diffuse radio–halo. Our analysis is based on new redshift data for 27 galaxies in the cluster region, measured from spectra obtained at the TNG, with the addition of other 105 galaxies recovered from reduction of CFHT archive data in a cluster region of $\sim 5'$ radius ($\sim 0.8 h^{-1}$ Mpc at the cluster distance) centered on the cD galaxy. The investigation of the dynamical status is also performed by using X–ray data stored in the Chandra archive. Further, valuable information comes from other bands – optical photometric, infrared, and radio data – which are analyzed and/or discussed, too. We find that A2219 appears as a peak in the velocity space at $z = 0.225$, and select 113 cluster members. We compute a high value for the line–of–sight velocity dispersion, $\sigma_v = 1438_{-86}^{+109}$ km s⁻¹, consistent with the high average X–ray temperature of 10.3 keV. If dynamical equilibrium is assumed, the virial theorem leads to $M \sim 2.8 \times 10^{15} h^{-1} M_{\odot}$ for the global mass within the virial region. However, further investigation based on both optical and X–ray data shows significant signs of a young dynamical status. In fact, we find strong evidence for the elongation of the cluster in the SE–NW direction coupled with a significant velocity gradient, as well as for the presence of substructure both in optical data and X–ray data. Moreover, we point out the presence of several active galaxies. We discuss the results of our multi–wavelength investigation suggesting a complex merging scenario where the main, original structure is subject to an ongoing merger with few clumps aligned in a filament in the foreground oriented along an oblique direction with respect to the line–of–sight. Our conclusion supports the view of the connection between extended radio emission and merging phenomena in galaxy clusters.

Key words. Galaxies: clusters: general – Galaxies: clusters: individual: Abell 2219 – Galaxies: distances and redshifts – intergalactic medium – Cosmology: observations

1. Introduction

In the hierarchical scenario for large–scale–structure formation, mergers are an essential ingredient of galaxy cluster evolution (e.g., White 1997; Evrard & Gioia 2002).

One of the most recent aspects of the merging phenomenology is the possible connection of cluster mergers with the presence of extended, diffuse radio sources, halos and relics (Feretti 1999; Buote 2002; Giovannini & Feretti 2002). Radio–halos are located at the cluster center, with typical sizes of $0.5 h^{-1}$ Mpc, regular shape, steep radio spectra and no significant polarization; while relics are lo-

Send offprint requests to: W. Boschin

[★] Based on observations made on the island of La Palma with the Italian Telescopio Nazionale Galileo (TNG) operated by the Centro Galileo Galilei of the INAF (Istituto Nazionale di Astrofisica) and with the 1.0m Jacobus Kapteyn Telescope (JKT) operated by the Isaac Newton Group at the Spanish Observatorio de Roque de los Muchachos of the Instituto de Astrofísica de Canarias.

cated in peripheral regions of the clusters, with irregular shape and generally highly polarized spectra (e.g., Feretti & Giovannini 1996; Giovannini & Feretti 2002). The synchrotron radio emission of halos and relics demonstrates the existence of large scale cluster magnetic fields, of the order of $0.1\text{--}1\ \mu\text{G}$, and of widespread relativistic particles of energy density $10^{-14} - 10^{-13}\ \text{erg cm}^{-3}$. Although the properties of halos and relics are not well understood, several suggestions for the mechanism transferring energy to the relativistic electrons have been made (e.g., Ensslin 2000).

Cluster mergers were suggested to provide the large amount of energy necessary for electron re-acceleration and magnetic field amplification (Feretti 1999; Feretti 2002; Sarazin 2002). However, the precise radio-halo formation scenario is still debated (e.g., Ensslin & Röttgering 2002). In fact, the diffuse radio sources are quite uncommon and only recently we can study these phenomena on the basis of a sufficient statistics (~ 30 clusters up to $z \sim 0.3$, e.g., Giovannini et al. 1999; see also Giovannini & Feretti 2002).

Presently, growing evidence of connection between diffuse emission and cluster merging is based on X-ray data (e.g., Böhringer & Schuecker 2002; Buote 2002). Studies based on a large number of clusters have found a significant relation between the radio and the X-ray surface brightness (Govoni et al. 2001) and connections between the presence of radio-halos/relics and irregular and bimodal X-ray surface brightness distribution (Schuecker et al. 2001). However, we are far from understanding the whole picture. Unfortunately, to date optical data is lacking or poorly exploited. Sparse literature concerns some few individual clusters (e.g., Colless & Dunn 1996; Gómez et al. 2000; Barrena et al. 2002; Mercurio et al. 2003).

Optical data are a powerful way to investigate the presence and the dynamics of cluster mergers (e.g., Girardi & Biviano 2002), too. The spatial and kinematic analysis of member galaxies allow us to detect and measure the amount of substructure, to identify and analyze possible pre-merging clumps or merger remnants. This optical information is really complementary to X-ray information since galaxies and ICM react on different time scales during a merger (see numerical simulations by Roettiger et al. 1997). Moreover, additional information comes from spectral types of member galaxies, since cluster mergers could stimulate star formation in cluster galaxies; thus the spectral signatures of past activity are useful to determine the relevant time-scales (e.g., Bekki 1999; Terlevich et al. 1999).

To investigate the connection between diffuse radio sources and cluster mergers, we have performed spectroscopic observations at TNG and a multi-wavelength analysis of the Abell cluster A2219 (Abell et al. 1989). This cluster shows the presence of a powerful radio-halo (Giovannini et al. 1999; Bacchi et al. 2003) and is a rich, X-ray luminous, hot cluster at moderate redshift $z \sim 0.22$ – Abell richness = 3 (Abell et al. 1989); $L_X(0.1\text{--}2.4\ \text{keV}) \sim 5 \times 10^{44}\ h^{-2}\ \text{erg s}^{-1}$ (Ebeling et al. 1996); $T_X \sim 10$

keV (Rizza et al. 1998). Possible evidence of the young dynamical status of A2219 comes from the ROSAT/HRI X-ray data analysis and strong/weak lensing features (Rizza et al. 1998; Smail et al. 1995; Dahle et al. 2002).

This paper is organized as follows. We present the new redshift data of A2219 in Sect. 2 and the analysis of optical data in Sect. 3. Our analysis of recent X-ray Chandra archival data is shown in Sect. 4. Active galaxies are analyzed and discussed on the basis of multi-wavelength data using also mid-IR and radio data in Sect. 5. Finally, in Sect. 6, we summarize and discuss our results suggesting a tentative picture of the dynamical status of A2219.

Unless otherwise stated, we give errors at the 68% confidence level (hereafter c.l.)

Throughout the paper, we assume a flat cosmology with $\Omega_m = 0.3$ and $\Omega_\Lambda = 0.7$. For the sake of simplicity in rescaling we adopt a Hubble constant of $100\ \text{km s}^{-1}\ h^{-1}$ Mpc. In this context, $1'$ corresponds to $\sim 0.152\ h^{-1}$ Mpc.

2. Optical observations and data reduction

Multi-object spectroscopic observations of A2219 were carried out at the TNG telescope in May 2003 during the program of proposal AOT-7 ID:18. We used DOLORES/MOS with the LR-B Grism 1, yielding a dispersion of $187\ \text{\AA}/\text{mm}$, and the Loral CCD of 2048×2048 pixels (pixel size of $15\ \mu\text{m}$). This combination of grating and detector results in dispersions of $2.8\ \text{\AA}/\text{pix}$. We have taken 1 MOS mask with 39 slits. We acquired two exposures of 1800.0 s each. Wavelength calibration was done using arc lamps before or after each exposure (Helium-Argon).

Reduction of spectroscopic data was carried out with IRAF¹. The signal-to-noise ratio per pixel was computed from the ratio between the signal at $6000\ \text{\AA}$ and the *rms* noise within $4000\text{--}7000\ \text{\AA}$. The resulting average signal-to-noise ratio of our spectra is $S/N \sim 16$.

Radial velocities are determined using the cross-correlation technique (Tonry & Davis 1979) implemented in the RVSAO package (developed at the Smithsonian Astrophysical Observatory Telescope Data Center). Each spectrum is correlated against six templates for a variety of galaxy spectral types: E, S0, Sa, Sb, Sc, Ir (Kennicutt 1992). The template producing the highest value of \mathcal{R} , i.e., the parameter given by RVSAO and related to the signal-to-noise of the correlation peak, is chosen. Moreover, all spectra and their best correlation functions are examined visually to verify the redshift determination. In some ambiguous cases, generally very late type galaxies, we use EMSAO package to confirm the estimated redshift, and in two cases we take the EMSAO redshift as a more reliable estimate of the redshift.

Out of the 39 spectra of objects, 9 turned out to be objects at $z \sim 0$ (included alignment stars for masks),

¹ IRAF is distributed by the National Optical Astronomy Observatories, which are operated by the Association of Universities for Research in Astronomy, Inc., under cooperative agreement with the National Science Foundation.

while for 3 cases, with $\mathcal{R} \lesssim 4$, we cannot determine the redshift. Thus, we obtain spectra for 27 galaxies.

We added to our data observations stored in CFHT archive (proposal ID: 01AF37, P.I.: J.P. Kneib): 1 MOS mask of one 1800 s –exposure with 155 slits. We reduced the spectra with the same procedure adopted for TNG ones. We succeeded in obtaining spectra for 111 galaxies, 6 of which are in common with TNG galaxies. The average S/N of these CFHT spectra is 8.

In order to combine our TNG data with those from CFHT archive, we have to check for a possible zero-point correction. To this aim we use the six galaxies with double redshift determination. This allow us to obtain a more rigorous estimate for the redshift errors since the nominal errors as given by the cross-correlation are known to be smaller than the true errors (e.g., Malamuth et al. 1992; Bardelli et al. 1994; Ellingson & Yee 1994; Quintana et al. 2000). Thus, for the six galaxies with double redshift determination, we fit the first determination vs. the second one by using a straight line and considering errors in both coordinates (e.g., Press et al. 1992). The fitted line agrees with the one to one relation (slope= 0.996 ± 0.004 , intercept= $(1 \pm 1) \times 10^{-3}$), but the small value of χ^2 –probability indicates a poor fit, suggesting that the nominal cross-correlation errors are underestimated. Only when nominal errors are multiplied by a ~ 2.3 factor the observed scatter can be explained. Therefore, hereafter we assume that true errors are larger than nominal cross-correlation errors by a factor 2.3. Slightly smaller correction factors are obtained for nearby clusters (e.g., Malamuth et al. 1992; Bardelli et al. 1994; Quintana et al. 2000).

Our spectroscopic catalogue consists of 132 galaxies sampling a cluster region of $5'$ around the dominant galaxy (no. 65), which is a cD galaxy (e.g., Allen et al. 1992).

We also determined the equivalent widths (EW hereafter) of the emission line [OII] and the absorption line $H\delta$, which are good indicators of current and recent star formation, respectively. Hereafter all the EW are in angstroms and are positive if the line is in absorption and negative if the line is in emission. We estimate minimum measurable EW as the width of a line spanning 2.8 \AA (our dispersion) in wavelength, with an intensity three times the rms noise in the adjacent continuum.

A variety of spectroscopic-classification schemes are presented in the literature (see, e.g., Couch et al. 1994; Dressler et al. 1999 and refs. therein). We use a conservative approach leading to a sparse classification (45% of the sample, see Table 1). We define *e*-type galaxies those showing strong active star formation as indicated by the presence of an [OII] line with an equivalent width of $\text{EW}([\text{OII}]) \lesssim -15 \text{ \AA}$ (e.g., Hammer et al. 1997; Postman et al. 1998). Out of galaxies having $S/N > 10$ we define *a*-type, those with strong Balmer absorption $\text{EW}(H\delta) > 4 \text{ \AA}$ (e.g., the “post-starburst” galaxies by Couch et al. 1994). We find fourteen “active” galaxies: four of *e*-type — measured $\text{EW}([\text{OII}])$ in the range $[-39.3, -14.3] \text{ \AA}$; ten of *a*-type — measured $\text{EW}(H\delta)$ in the range $[4.0; 12.4] \text{ \AA}$.

Out of non active galaxies with $S/N > 10$ those (37) with measured $\text{EW}(H\delta) < 3 \text{ \AA}$ are classified as passive galaxies (*k*-type) and the remaining nine galaxies, intermediate between *a* and *k* are classified as *i*-type. Non active galaxies do not show significant [OII] emission and only two *a*-galaxies show a very small [OII] emission (-3.5 \AA).

As far as photometry is concerned, we obtained exposures on a $10' \times 10'$ unvignetted field centered on $\alpha = 16^{\text{h}} 40^{\text{m}} 22^{\text{s}}$, $\delta = 46^{\circ} 42' 15''$ (J2000) through B and R Harris filters using the CCD camera mounted on the 1m JKT telescope (at Roque de los Muchachos Observatory, La Palma) in July 2003. We performed several exposures for total integration times of 3000 and 7200 s in R and B band, respectively, with seeing conditions about $1.4''$. We carried out the image reduction (bias, flat and fringing corrections) using IRAF package and photometry using AUTOMAG SExtractor procedure (Bertin & Arnouts 1996). This photometry was calibrated using Landolt’s standard fields at the JKT and TNG telescopes and transformed into the Johnson filter system. We estimate that our photometric sample is complete down to $R = 19.7$ and $B = 21.4$ within the observed field.

We assign R magnitudes to 131 out of the 132 galaxies of our spectroscopic catalogue: the only exception is galaxy no. 52, which is too close to a very bright star. Out of these 131 galaxies, 129 have assigned magnitudes in B band, too. We measure redshift for galaxies down to $R \sim 20.5$ mag, but a high level of completeness is obtained only for bright galaxies ($\sim 66\%$ completeness for $R < 19.7$ mag).

Table 1 lists the velocity catalogue² (see also Fig. 1): identification number of each galaxy, ID (Column 1); right ascension and declination, α and δ (J2000, Column 2); R magnitudes (Column 3); B–R colours (Column 4); heliocentric radial velocities, $v = cz_{\odot}$ (in km s^{-1} , Column 5) with assumed errors, Δv , i.e., the nominal ones given by cross-correlation technique multiplied by 2.3 (Column 6); the code for the spectral classification SC, where “I” and “R” indicate mid-IR and radio emitting galaxies, respectively (see Sect. 5), (Column 7); the telescope used to obtain the spectra (Column 8, T and C indicate TNG and CFHT, respectively).

3. Optical analysis

3.1. Member selection and global properties

According to the analysis of the redshift distribution based on the one-dimensional adaptive kernel technique (Pisani 1993, see also Fadda et al.’s 1996 and Girardi et al. 1996) A2219 appears as a peak at $z \sim 0.225$ in redshift space (Fig. 2). Out of 132 galaxies with redshift, fourteen are foreground objects and three are background objects. In particular, the foreground galaxies form two peaks, one of six galaxies at $z \sim 0.11$ and one of eight galaxies at $z \sim 0.19$.

² The coordinates of non-galaxy objects are available upon request.

Table 1. Velocity catalog of 132 spectroscopically measured galaxies. in Column 1, IDs in italics indicate non-cluster galaxies.

ID	α, δ (J2000) $16^h, +46^\circ$	R	B - R	v (km s ⁻¹)	Δv	SC	Tel.
1	39 54.53, 40 16.4	19.89	2.15	67614	223		C
2	39 55.54, 41 01.4	18.80	1.80	68948	117	<i>a</i>	C
3	39 55.94, 42 28.7	17.89	1.11	33327	205	<i>k</i>	C
4	39 56.69, 41 40.4	18.89	2.26	67403	97		C
5	39 56.76, 43 35.4	18.19	2.34	68244	87	<i>k</i>	C
6	39 56.88, 40 24.1	18.33	2.11	53453	71	<i>k</i>	C
7	39 59.26, 41 42.0	19.83	2.11	69556	248		C
8	39 59.66, 44 24.0	18.80	1.95	67681	85	<i>i</i>	C
9	40 01.63, 41 50.6	19.68	1.62	69022	198		C
10	40 02.78, 44 15.3	19.73	2.14	67205	198		C
11	40 03.19, 41 53.7	18.79	2.19	68023	152		C
12	40 03.36, 43 58.8	18.74	2.43	66980	108		C
13	40 03.50, 41 38.0	19.91	1.70	68235	92	<i>a</i>	T
14	40 03.70, 46 37.5	18.07	2.20	70167	136	<i>i</i>	C
15	40 03.91, 40 45.8	20.07	2.35	67995	85	<i>k</i>	T
16	40 04.06, 44 05.7	19.57	2.20	67483	145		C
17	40 04.10, 46 45.2	18.27	1.81	69424	244	<i>i</i>	C
18	40 04.15, 40 57.4	19.43	1.09	33073	191	<i>k</i>	T
19	40 04.39, 42 08.6	18.46	2.18	64785	94		C
20	40 04.92, 42 00.2	19.80	1.65	67906	136		C
21	40 05.93, 42 04.0	19.14	1.39	67488	156		C
22	40 06.19, 44 19.5	19.40	2.06	67739	106		C
23	40 06.46, 46 25.9	17.53	1.85	43521	138	<i>k</i>	C
24	40 06.72, 40 40.2	18.21	2.31	68595	69		C
25	40 07.15, 41 06.5	18.53	1.99	65555	156		C
26	40 07.27, 45 30.5	18.92	2.11	68483	106		C
27	40 08.66, 41 42.9	19.52	1.52	57266	163	<i>i</i>	C
28	40 08.81, 43 40.6	18.78	2.37	69612	60	<i>k</i>	C
29	40 09.12, 45 48.7	19.33	1.60	68317	92		C
30	40 09.14, 41 52.5	19.54	2.07	65020	133		C
31	40 09.17, 42 11.3	19.98	2.02	70704	108		T
32	40 09.46, 43 32.8	18.99	1.58	67772	122	<i>a</i>	C
33	40 09.65, 43 03.2	19.86	2.33	67773	81	<i>k</i>	T
34	40 10.20, 45 32.1	18.91	2.35	70238	143		C
35	40 10.63, 43 22.5	18.74	2.08	70212	83	<i>a</i>	C
36	40 11.47, 42 31.2	19.74	2.18	70824	90	<i>k</i>	T
37	40 11.52, 43 19.8	18.61	2.30	67655	83	<i>k</i>	C
38	40 11.76, 38 53.9	20.06	1.61	106730	168	<i>e</i>	T
39	40 12.53, 41 59.6	19.41	2.09	66638	62	<i>k</i>	T
40	40 12.55, 45 35.0	20.12	1.97	66657	129		C
41	40 12.74, 41 10.6	18.02	2.11	70175	64	<i>k</i>	C

Table 1. Continued.

ID	α, δ (J2000) $16^h, +46^\circ$	R	B - R	v (km s ⁻¹)	Δv	SC	Tel.
42	40 13.10, 43 06.2	18.82	1.26	69084	69	<i>a, I</i>	C
43	40 13.18, 44 40.5	18.13	2.21	67154	67	<i>i</i>	C
44	40 13.80, 44 50.6	19.81	2.13	67068	140		C
45	40 14.04, 41 49.5	17.44	1.41	33192	97	<i>k, I</i>	C
46	40 14.26, 43 04.9	18.89	2.22	67587	83		C
47	40 14.35, 43 52.9	19.44	1.73	66045	94	<i>k</i>	T
48	40 14.42, 46 14.7	18.84	2.13	65166	117		C
49	40 14.64, 43 04.4	19.96	1.98	67437	163		C
50	40 15.70, 45 48.6	19.38	2.32	69168	143		C
51	40 15.89, 42 31.5	18.54	2.11	68411	85	<i>i, R</i>	C
52	40 16.10, 44 12.4	69563	78	<i>i</i>	C
53	40 16.20, 40 20.8	20.21	1.65	68334	110	<i>a</i>	T
54	40 16.66, 46 06.7	19.06	2.30	69540	186		C
55	40 16.68, 43 09.4	20.35	2.20	67937	255		C
56	40 16.92, 42 47.9	19.98	2.33	68319	90	<i>k</i>	T
57	40 16.97, 39 50.7	20.38	0.39	64664	186		C
58	40 17.18, 42 11.3	19.03	1.88	66799	147		C
59	40 17.95, 44 38.4	19.81	1.85	67744	108		C
60	40 18.19, 42 36.0	18.28	2.70	69246	97		C
61	40 18.36, 40 21.3	17.30	1.71	56619	62	<i>i</i>	C
62	40 19.13, 42 41.5	19.24	1.26	68558	168		C
63	40 19.25, 40 08.8	19.10	1.24	68590	51	<i>k</i>	T
64	40 19.39, 41 05.5	19.07	2.16	66975	90		C
65	40 19.87, 42 41.3	16.19	2.10	67259	71	<i>k</i>	T
66	40 19.97, 38 41.3	18.48	2.27	68681	106		C
67	40 20.38, 40 12.5	18.13	1.72	57334	64	<i>k</i>	C
68	40 20.57, 41 48.7	18.47	2.35	70232	51	<i>k</i>	T
69	40 20.70, 45 51.7	19.47	2.29	67345	140		C
70	40 20.81, 42 43.9	18.69	1.54	66330	74		C
71	40 21.50, 42 39.3	17.78	1.98	65490	99		C
72	40 21.53, 40 48.4	18.41	1.46	56477	161	<i>I</i>	C
73	40 21.86, 41 16.5	18.36	1.80	55832	90	<i>k</i>	T
74	40 21.86, 43 58.4	18.87	2.15	66947	74	<i>k</i>	T
75	40 21.89, 44 44.3	18.44	2.09	64697	60	<i>k</i>	C
76	40 21.96, 46 17.9	19.06	1.72	64878	108	<i>a</i>	C
77	40 22.08, 42 46.0	17.42	2.23	62364	99	<i>k, R</i>	C
78	40 22.08, 43 07.6	19.67	2.15	67529	97	<i>k</i>	T
79	40 22.20, 45 56.4	19.82	2.03	65624	122	<i>k</i>	T
80	40 22.80, 39 52.0	20.61	2.88	64953	173		C
81	40 22.90, 42 17.9	17.83	1.64	65516	83	<i>a, I</i>	C
82	40 23.30, 46 33.0	16.20	1.45	32860	97	<i>k</i>	C
83	40 23.40, 44 53.0	20.71	1.72	68327	179		T

of $M(< R_{\text{vir}}) = 2.8_{-0.7}^{+0.8} \times 10^{15} h^{-1} M_{\odot}$, (Girardi et al. 1998; Girardi & Mezzetti 2001).

The high value of σ_v is confirmed also if we apply a tighter member selection (i.e., using a bin of $0.25 h^{-1}$ Mpc in the shifting gapper): only another three galaxies are rejected –those with the lowest velocities– resulting in $\sigma_v = 1355_{-82}^{+82} \text{ km s}^{-1}$ for the remaining galaxies. Moreover, we compute the differential and integral mean velocity and velocity dispersion profiles in Fig. 4: this analysis shows

that the global values of \bar{v} and σ_v are already reached within the central cluster region of $0.1\text{--}0.2 h^{-1}$ Mpc. The conclusion of the above analyses is that contamination by obvious field interlopers and/or close cluster companions cannot explain the high value of the global velocity dispersion. More probably, this value is connected with the peculiarity of the internal dynamics of the cluster itself, which will be analyzed below.

Table 1. Continued.

ID	α, δ (J2000) 16 ^h , +46°	R	B - R	v (km s ⁻¹)	Δv	SC	Tel.
84	40 23.60, 40 32.0	18.93	2.29	69604	74		C
85	40 23.70, 42 10.0	17.16	2.45	68579	85	<i>k, R</i>	C
86	40 23.70, 43 05.0	18.23	2.38	69673	83	<i>k</i>	T
87	40 23.80, 43 20.0	18.88	2.37	66376	60	<i>k</i>	T
88	40 24.55, 42 22.1	18.94	2.22	66053	78	<i>k</i>	C
89	40 24.79, 40 38.0	20.79	1.81	69885	150		C
90	40 25.01, 44 18.9	18.28	1.52	40362	136		C
91	40 25.39, 44 10.5	19.60	2.30	67633	154		C
92	40 25.54, 43 42.8	18.71	2.13	66346	69	<i>k</i>	T
93	40 25.80, 42 34.7	17.99	2.10	63015	81	<i>i</i>	C
94	40 25.87, 40 34.1	18.66	1.52	68027	145		C
95	40 26.64, 44 13.9	19.60	2.24	67488	110		C
96	40 26.95, 45 43.7	20.64	1.78	70934	235		C
97	40 27.65, 46 23.1	18.85	2.23	67814	92		C
98	40 28.30, 41 46.4	19.81	2.27	66766	106	<i>k</i>	T
99	40 28.51, 46 02.6	17.56	1.58	64402	81	<i>a</i>	C
100	40 29.35, 46 22.4	19.48	2.21	67825	110		C
101	40 29.74, 42 31.7	19.93	1.98	63681	196		C
102	40 30.70, 41 46.6	19.02	2.20	67255	71		C
103	40 31.87, 40 45.6	18.79	1.43	69097	140		C
104	40 31.94, 42 30.5	17.59	1.85	72697	78	<i>i</i>	C
105	40 32.09, 46 36.8	19.03	64928	74		C
106	40 32.93, 46 45.9	17.46	66408	51	<i>k</i>	C
107	40 33.00, 45 01.1	18.55	2.27	67758	81	<i>k</i>	T
108	40 33.29, 43 49.1	19.98	1.77	67462	113	<i>k</i>	T
109	40 33.74, 40 31.2	19.60	0.49	70574	175		C
110	40 34.25, 39 03.9	19.43	1.48	65715	97		C
111	40 35.11, 44 45.1	18.70	2.10	68703	159		C
112	40 35.62, 41 28.8	19.24	2.41	66630	94		C
113	40 36.41, 44 18.3	18.77	2.11	70142	78		C
114	40 36.96, 42 29.0	19.90	2.03	64736	205		C
115	40 37.63, 44 30.0	19.92	2.20	122821	179		T
116	40 37.66, 38 58.7	18.60	1.52	79042	92	<i>e</i>	C
117	40 37.82, 45 08.8	18.10	3.09	61291	156		C
118	40 37.94, 42 46.8	19.36	2.16	65551	136		C
119	40 38.45, 43 47.9	19.62	1.42	65813	78	<i>a</i>	C
120	40 38.57, 42 35.4	20.35	2.27	67301	170		T
121	40 38.88, 40 20.7	18.94	1.66	57095	207		C
122	40 39.36, 42 52.3	18.88	2.09	66992	83		C
123	40 39.72, 39 07.0	17.70	2.22	67564	101	<i>k</i>	C
124	40 39.86, 44 45.3	19.40	2.02	64910	81		C
125	40 41.11, 40 10.9	19.78	2.09	66389	235		C
126	40 41.74, 40 23.4	19.31	2.25	67194	152		C
127	40 42.74, 41 30.0	19.76	1.43	68626	202		C
128	40 43.46, 44 44.9	20.28	2.03	65829	156		C
129	40 44.42, 40 19.2	19.52	2.14	67997	147		C
130	40 45.62, 43 26.5	20.21	1.04	65784	154	<i>e</i>	C
131	40 45.86, 44 59.3	20.18	1.46	57661	182	<i>e</i>	C
132	40 48.00, 41 56.5	19.94	2.22	66938	196		C

Note. The velocities and nominal cross-correlation errors (in km sec⁻¹) for 6 galaxies spectroscopically observed both with the TNG and the CFHT, respectively, are given below:

#38 (106730±73; 106738±148); #53 (68334±48; 68227±59);
#65 (67259±31; 67372±49); #98 (66766±46; 67074±49);
#107 (67758±35; 67921±46); #108 (67462±49; 67529±34).

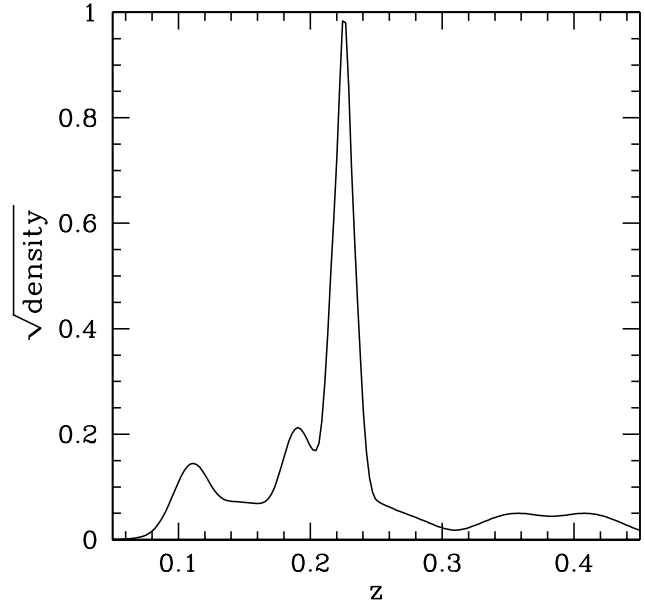


Fig. 2. Square root of the redshift galaxy density, as provided by the adaptive-kernel reconstruction method. Units on the y axis are arbitrary.

3.2. Internal dynamics

As a first step in the study of internal dynamics we analyze the velocity distribution. We consider three estimators of Gaussianity: the kurtosis; the skewness, and the scaled tail index (see, e.g., Beers et al. 1991). We find no significant evidence that the velocity distribution differs from a Gaussian. Moreover, we do not find any evidence of a peculiar velocity of the cD galaxy with respect to the average velocity of cluster members (see Gebhardt & Beers 1991).

In order to investigate the velocity field we divide galaxies in a low and a high-velocity samples by using the median cluster velocity and check the difference between the two distributions of galaxy positions. Fig. 5 shows that low and high-velocity galaxies are segregated roughly along the E-W direction. The two distributions are different at the 99.6% c.l. according to the two-dimensional Kolmogorov-Smirnov test (hereafter 2DKS-test; see Fasano & Franceschini 1987, as implemented by Press et al. 1992). In order to estimate the direction of the velocity gradient we perform a multiple linear regression fit to the observed velocities with respect to the galaxy positions in the plane of the sky (see also den Hartog & Katgert 1996; Girardi et al. 1996): we find a PA = 79^{+22}_{-20} degrees (measured counter-clock-wise from the North, see Fig. 5).

Moreover, we compute the mean velocity and LOS velocity dispersion separately for each one of the four samples corresponding to the NE, SE, SW and NW cluster sectors. Table 2 shows that mean velocities are larger in the Western than in the Eastern sectors in agreement with

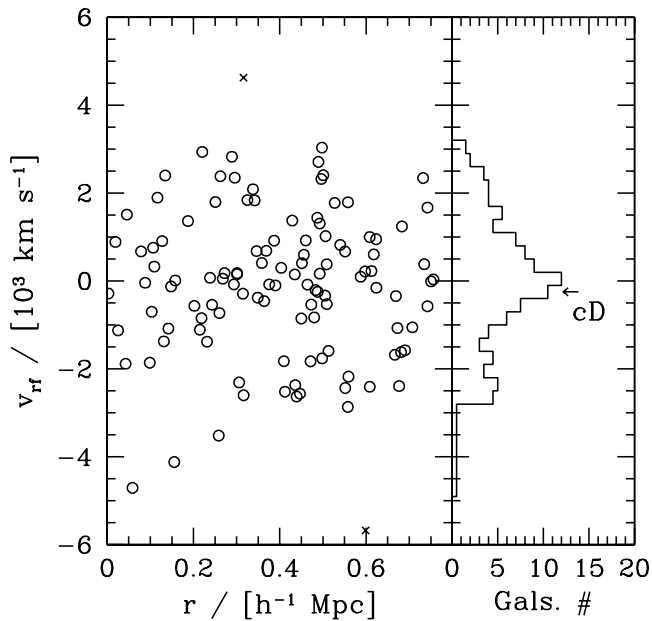


Fig. 3. Left panel: rest-frame velocities v_{rf} vs. projected cluster-centric distance r of galaxies in the main peak of Fig. 2. Circles indicate cluster members; crosses indicate the two galaxies rejected by the “shifting gapper” procedure. Right panel: histogram of rest-frame velocities of selected 113 cluster members. The arrow indicates the cD galaxy velocity.

Table 2. Mean galaxy velocities and velocity dispersion (in km s^{-1}) in four cluster sectors (see text). N indicates the number of member galaxies in each sector.

Sector	N	\bar{v}	σ_v
NE	30	66712 ± 272	1458^{+305}_{-172}
SE	26	67213 ± 330	1642^{+271}_{-152}
SW	25	68007 ± 288	1403^{+248}_{-224}
NW	31	68128 ± 187	1018^{+161}_{-109}

the above analyses. As for σ_v , this is largest in the SE sector and smallest in the NW sector: the difference is significant at the 98.7% c.l. according to the F-test (Press et al. 1992).

To check for the presence of three-dimensional substructure we compute the Δ -statistics devised by Dressler & Schectman (1988) and establish its significance running 1000 Monte Carlo simulations, in which we randomly shuffle galaxy velocities. The signal of substructure is significant at the 95% c.l.. In Fig. 6 we plot the distribution on the sky of all galaxies, each marked by a circle: the larger the circle, the larger is the deviation δ_i of the local parameters from the global cluster parameters, i.e., there is more evidence for substructure. The most likely substructure

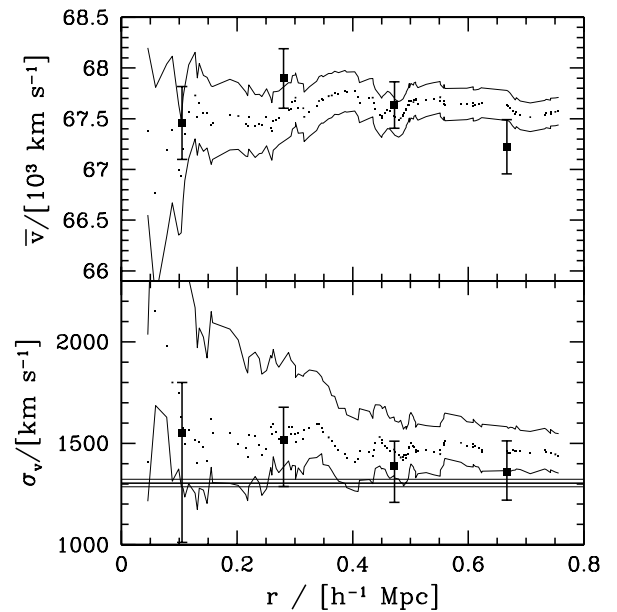


Fig. 4. Differential (big squares) and integral (small points) mean velocity and line-of-sight velocity dispersion profiles. For the differential profiles, the results for four annuli from the cluster center, each of $0.2 h^{-1} \text{Mpc}$, are shown. For the integral profiles, the mean and dispersion at a given (projected) radius from the cluster center is estimated by considering all galaxies within that radius. The error bands at the 68% c.l. are shown. In the lower panel, the horizontal lines represent X-ray temperature with the respective errors transformed in σ_v (assuming $\beta_{\text{spec}} = 1$ where $\beta_{\text{spec}} = \sigma_v^2 / (kT_X / \mu m_p)$, with μ the mean molecular weight, m_p the proton mass, and T_X the X-ray temperature).

ture lies close to the cluster center roughly to the SE of the cD galaxy.

3.3. Colour segregation and 2-D galaxy distribution

We check for possible colour segregation of galaxies by using the 110 member galaxies for which we have B–R colours. We obtain a correlation between $|v_{\text{rf}}|$ and colour (at the 96.3% c.l.). We divide the sample in two subsamples with colours bluer and respectively redder than the median B–R colour=2.12. We obtain that the velocity dispersions of the two subsamples differ at the 99.5% c.l. ($\sigma_v = 1627^{+144}_{-96}$ and $\sigma_v = 1100^{+190}_{-160} \text{ km s}^{-1}$ for the B–R < 2.12 and B–R > 2.12 galaxies, respectively).

To further investigate the above difference we also use the colour–magnitude relation (hereafter CMR), which indicates the early-type galaxy locus,

$$B - R = 2.976 - 0.041 \cdot R, \quad (1)$$

obtained by using a 2 sigma-clipping fitting procedure (see Fig. 7). Blue objects are defined to be those galaxies at least 0.25 mag bluer in B–R than the colour of the

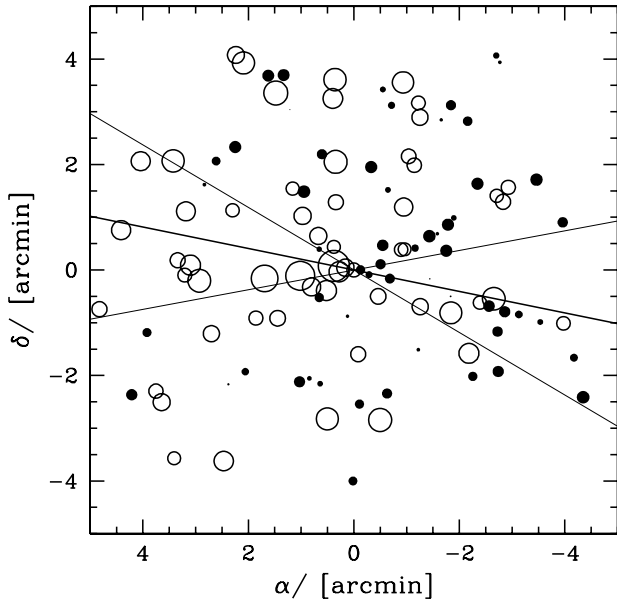


Fig. 5. Spatial distribution on the sky of 113 cluster members. Open and solid circles indicate low- and high-velocity galaxies: the larger the symbol, the smaller is the radial velocity. The plot is centered on the cluster center (coincident with the cD galaxy). The solid and faint lines indicate the position angle of the cluster velocity gradient and relative errors, respectively.

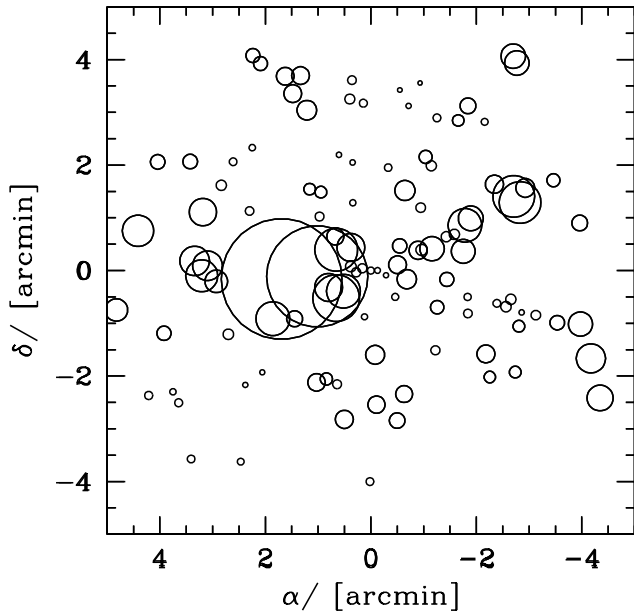


Fig. 6. Spatial distribution on the sky of the 113 cluster members, each marked by a circle: the larger the circle, there is more evidence for substructure (according to the Dressler & Schectman test, see text). The plot is centered on the cluster center.

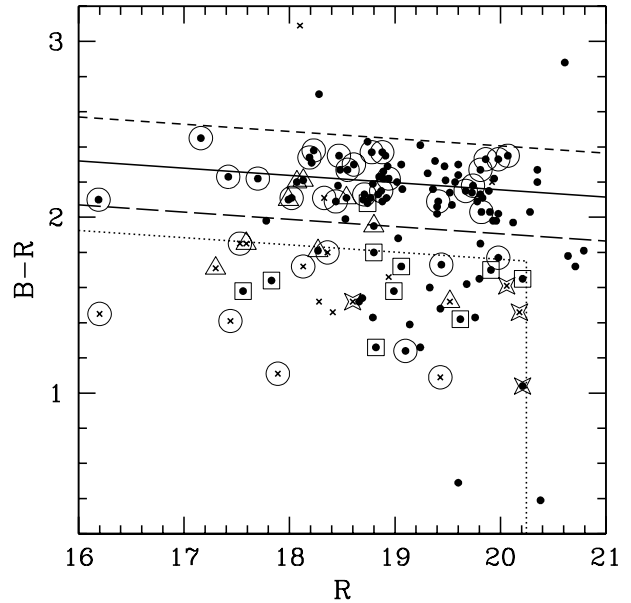


Fig. 7. B-R vs. R diagram for galaxies with available spectroscopy: small dots and crosses denote cluster and field members, respectively. Large symbols denotes spectroscopically classified galaxies: circles, triangles, squares, and stars indicate k -, i -, a -, and e -galaxies, respectively. The solid line gives the best-fit CMR; the dashed lines are drawn at ± 0.25 mag from the CMR. According to our working definition in Sect. 3.3 cluster members are divided in: *blue* and *red* galaxies (below and above the long-dashed line, respectively); *very red* galaxies lie above the solid line. The left-down region delimited by the dotted lines defines the locus of Butcher-Oemler galaxies (Sect. 5).

CMR. These *blue* galaxies have typically $B-R < 2$, thus include Sa spiral galaxies and exclude elliptical galaxies (according to the expected typical colours). The remaining objects, which we define the *red* sample, should consist most of ellipticals and lenticulars. Moreover, we further divide *red* galaxies in two subsamples: *very red* and *not-very red* galaxies, depending on their location above or below the CMR. Table 3 shows \bar{v} and σ_v estimates for *blue* and *red* galaxies, and separately for *very* and *not-very red* galaxies. We point out that the populations of *very red* and *not-very red* galaxies are different. In fact, the σ_v of *not-very red* galaxies is larger than the σ_v of *very red* ones (at the 99.5% c.l. according to the F-test). Moreover, the mean velocity of *not-very red* galaxies is smaller than that of *very red* ones (at the 99.5% c.l. according to the mean-test).

We also analyze the two-dimensional spatial distribution of galaxies. First, we consider bright cluster members, i.e. the sample of 80 galaxies with $R < 19.7$ for which we have a good level of spatial completeness (see Sect. 2). Fig. 8 shows the presence of two clumps in the cluster center which defines a SE-NW elongated structure ($PA \sim 110^\circ$): the main peak roughly coincides with the cD

Table 3. Mean velocities and velocity dispersions (in km s^{-1}) for galaxies with different colors (see text). N is the number of galaxies of each type.

Population	N	\bar{v}	σ_v
blue galaxies	33	67676 ± 255	1439^{+177}_{-139}
red galaxies	77	67568 ± 163	1423^{+146}_{-123}
(not very) red galaxies	40	66942 ± 265	1655^{+215}_{-168}
(very) red galaxies	37	67969 ± 173	1032^{+172}_{-126}

position, and the secondary peak – at the West – traces the filament of high velocity galaxies well visible in Fig. 1 (from no. 49 to no. 28). The cD also shows an elongation in the SE–NW direction described by the position angle on the celestial sphere $\text{PA} = 114 \pm 3$ degrees (Smail et al. 1995).

Then, to study fainter galaxies and to work with a much more robust statistics, we consider the B and I photometric data of Smail et al. (1998) and define likely members using the CMR. Specifically, we select 484 likely cluster members considering objects ($I < 22$, stellar index < 0.9) within 0.25 mag from the $B - I = 5.398 - 0.115 \cdot I$. The top panel of Fig. 9 shows a main structure centered on the cD galaxy and elongated in the SE–NW direction, with a PA of $\sim 110^\circ$ for the central region (along the filament described above) and a larger PA for the external region. A similar structure is also traced by the subsample of very red galaxies – those above the CMR (Fig. 9 middle panel). Instead, the distribution of not very red galaxies shows three main clumps aligned in the NE–SW direction (Fig. 9 bottom panel). In particular, the densest peak is located at about $1'$ South–East of the cD, in the position of the substructure suggested by the Dressler–Schectman test (Sect. 3.2).

4. X–ray observation and analysis

The X–ray analysis of A2219 is performed on the archival data of the Chandra ACIS–S observation 800072 (exposure ID #896, P.I.: J. Houck). The pointing has an exposure time of 42.8 ks. Data reduction is performed by using the package CIAO³ (Chandra Interactive Analysis of Observations) on chip S3 (field of view $\sim 8.5' \times 8.5'$). First, we remove events from the level 2 event list with a status not equal to zero and with grades one, five and seven. Then, we select all events with energy between 0.3 and 10 keV. In addition, we clean bad offsets and examine the data filtering out bad columns and removing times when the count rate exceeds three standard deviations from the mean count rate per 3.3 s interval. We then clean S3 chip for flickering pixels, i.e., times where a pixel has events in two sequential 3.3 s intervals. The resulting exposure time for the reduced data is 42.3 ks.

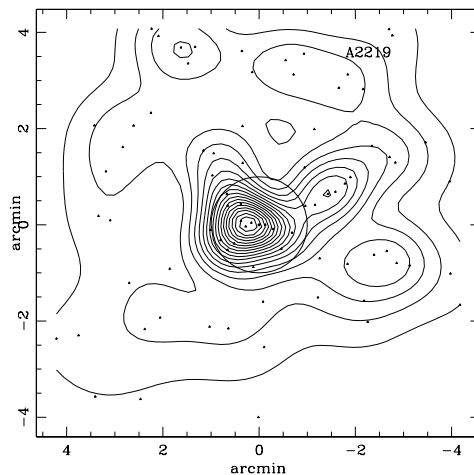


Fig. 8. Spatial distribution on the sky and relative iso-density contour map of 80 bright cluster ($R < 19.7$ galaxies), obtained with the adaptive–kernel method (cf. Pisani 1993,1996). The plots are centered on the cluster center. The $1'$ circle is centered on the cD galaxy.

In Fig. 10 we plot an R–band image of the cluster with superimposed the X–ray contour levels of the Chandra image and the radio contour levels of a low–resolution VLA image by Bacchi et al. (2003). The elongated shape of the cluster is clearly visible. By using the CIAO package Sherpa we fit an elliptical Beta model to the X–ray photon distribution to quantify the departure from the spherical shape. The model is defined as follows:

$$f(x, y) = f(r) = A/[1 + (r/r_0)^2]^\alpha \quad (2)$$

where the radial coordinate r is defined as $r(x, y) = [X^2(1 - \epsilon)^2 + Y^2]^{1/2}/(1 - \epsilon)$, $X = (x - x_0) \cos \theta + (y - y_0) \sin \theta$ and $Y = (y - y_0) \cos \theta - (x - x_0) \sin \theta$. Here x and y are physical pixel coordinates on chip S3. The best fit centroid position is located $12''$ South–East of the dominant galaxy. The best fit core radius, the ellipticity and the position angle are $r_0 = 69.7 \pm 1.3$ arcsec ($177 \pm 3 h^{-1}$ kpc), $\epsilon = 0.339 \pm 0.006$ and $\text{PA} = 128.8 \pm 0.6$ degrees, respectively. The elongated shape of the cluster is also in agreement with Rizza et al’s (1998) result, who found evidence of elongations and excesses in the X–ray emission relative to a circular model on ROSAT data (see their Table 7).

In order to detect possible substructures in A2219 we perform a wavelet analysis by running the task CIAO/Wavdetect on the chip S3. The task was run on different scales in order to search for substructures with different sizes. The significance threshold⁴ was set at 10^{-6} . The results are shown in Fig. 10. Thick ellipses represent four significant substructures found by Wavdetect.

⁴ see § 11.2 of the CIAO Detect Manual (software release version 2.2.1, available at the WWW site <http://cxc.harvard.edu/ciao/manuals.html>)

³ CIAO is freely available at <http://asc.harvard.edu/ciao/>

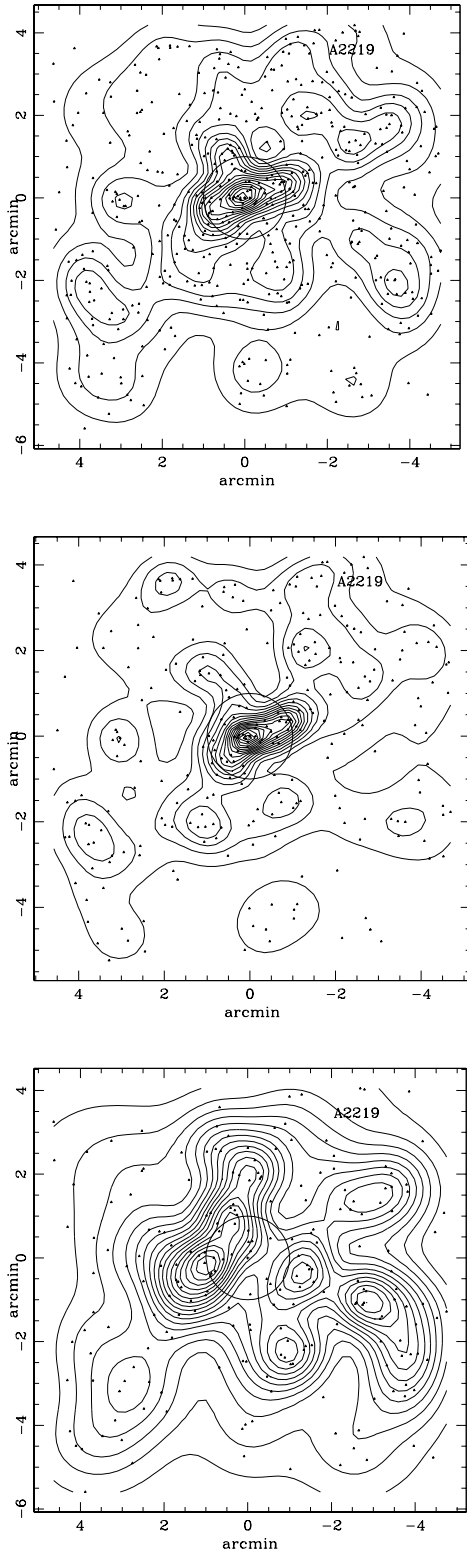


Fig. 9. Same as Fig. 8 but for likely cluster members selected on the basis of the B–I CMR in the photometric sample of Smail et al. (1998). Top panel: the 484 $I < 22$ galaxies. Middle and bottom panels: two subsamples corresponding to very red and not very red galaxies (273 and 211 galaxies, respectively).

The principal one, located at R.A. $16^{\text{h}} 40^{\text{m}} 20.1^{\text{s}}$ and Decl. $+46^{\circ} 42' 45''$, is centered on the cD galaxy. There are two more significant peaks in the core of the cluster located at R.A. $16^{\text{h}} 40^{\text{m}} 23.1^{\text{s}}$ and Decl. $+46^{\circ} 42' 19''$, and at R.A. $16^{\text{h}} 40^{\text{m}} 21.6^{\text{s}}$ and Decl. $+46^{\circ} 42' 26''$, respectively. Finally, outside the core, we find a fourth structure at R.A. $16^{\text{h}} 40^{\text{m}} 27.7^{\text{s}}$ and Decl. $+46^{\circ} 41' 13''$, about $2'$ South–East of the dominant galaxy. The presence of a photon excess in this position is also evident from Fig. 11, where we plot the residual map of the elliptical Beta model fit. A peak of positive residuals is observed at the position of the fourth structure.

Passing to the spectral analysis of the cluster X–ray photons, we first compute a global estimate of the ICM temperature. The temperature is computed from the spectrum of the cluster within a circular aperture of $3'$ radius around the cluster center. Fixing the absorbing galactic hydrogen column density at $1.75 \times 10^{20} \text{ cm}^{-2}$, computed from the HI maps by Dickey & Lockman (1990), we fit a Raymond–Smith (1977) spectrum using the CIAO package Sherpa with a χ^2 statistics. We find a best fitting temperature of $T_{\text{X}} = 10.3 \pm 0.3 \text{ keV}$, in agreement with previous estimates by Allen (2000) and White (2000).

To detect the possible presence of temperature gradients in the cluster we divide the cluster in eight sectors, as shown in Fig. 12, and compute the temperature in each of them. We find a temperature gradient from the cooler SE sectors to the hotter NW ones. This pattern is also confirmed by a softness ratio analysis of the Chandra image. We define the softness ratio as $SR \equiv (S - H)/(S + H)$, where S is the number count of photons with soft energies in the range 0.5–2 keV, while H is the number count of photons with hard energies in the range 2–7 keV. Then we count soft and hard photons in circles with 50 pixels aperture radius sliding on a 200×200 pixels grid. Background photon counts are subtracted by using an ACIS background event file by M. Markevitch. The background subtracted values of the softness ratios are plotted in Fig. 13. In this figure different grey levels identify regions with different SR s. High SR (lower temperature) regions are concentrated mainly in sectors 1, 2, 3 and 4, in agreement with the temperature map shown in Fig. 12.

5. Active galaxies

The star formation properties of the galaxies in our sample are examined on the basis of the spectral classification introduced in Sect. 2 (see Table 1). Out of 60 classified galaxies, 46 are member galaxies: 29/37 k –galaxies, 6/9 i –galaxies, 1/4 e –galaxy, and 10/10 a –galaxies. The relative fraction of cluster a –galaxies is 22%. For different $EW(\text{H}\delta)$ levels we find 13% and 37% (> 5 and $> 3 \text{ \AA}$, respectively). For comparison, Poggianti et al. (1999) found a 21% of $k+a/a+k$ galaxies with $EW(\text{H}\delta) > 3 \text{ \AA}$ and Balogh et al. (1999) found a fraction $\lesssim 4\%$ of $K+A$ with $EW(\text{H}\delta) > 5 \text{ \AA}$. An open question is whether or not strong $\text{H}\delta$ galaxies are typical of cluster environments (cf., e.g., Poggianti et al. 1999 with Balogh et al. 1999) since these galaxies

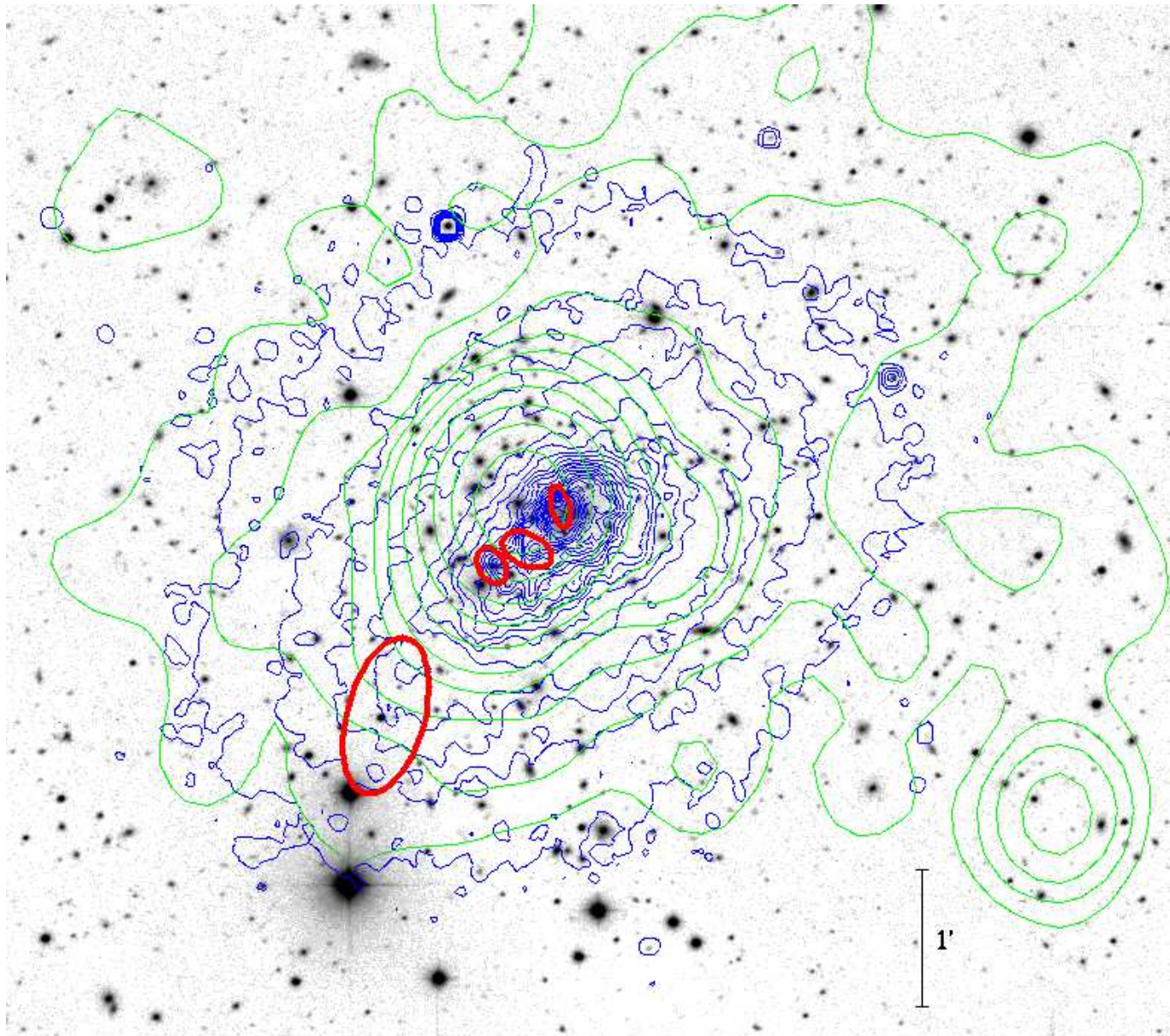


Fig. 10. R-band image of the cluster A2219 with, superimposed, the contour levels of the Chandra image (blue) and of a low-resolution VLA image (green) by Bacchi et al. (2003). The red ellipses represent the structures detected by Wavdetect. North is at top and East to left.

could be produced by a cluster merger (Bekki 1999). Very interestingly, we find 0/14 a -galaxies in the field against 10/46 in cluster environment.

We check for possible spectral segregations of cluster galaxies, both in position and in velocity space by comparing the dynamics of passive k -galaxies with that of active e - plus a -galaxies. We find a larger velocity dispersion in the case of active galaxies, but the difference is not significant. Moreover, we verify that the two subsamples do not differ in the distribution of galaxy positions by using the 2DKS-test. Fig. 14 shows the distribution of spectroscopically-classified galaxies: 4/25 and 7/21 are classified as active in the central and external cluster regions (within and outside $2'$). As for central active galax-

ies, three are located in the NW filament of high velocity galaxies in the central region, corresponding to the NW subclump identified in the two-dimensional analysis of Sect. 3.3. The fourth galaxy (no. 81) lies at the SE of the cD galaxy.

As for the interpretation of spectra, the only detected e -galaxy is very blue (the bluest within this sample) as generally found for starburst models. Nine of ten a -galaxies are classified as *blue* according to our definition (see Fig. 7). Thus their spectra can be explained by “post-starburst” models which reproduce strong $H\delta$ EW and no significant emission lines in a quiescent phase soon after a starburst (about between a few Myr and 1.5 Gyr; e.g., Poggianti et al. 1999). Alternatively, strong $H\delta$ EW could

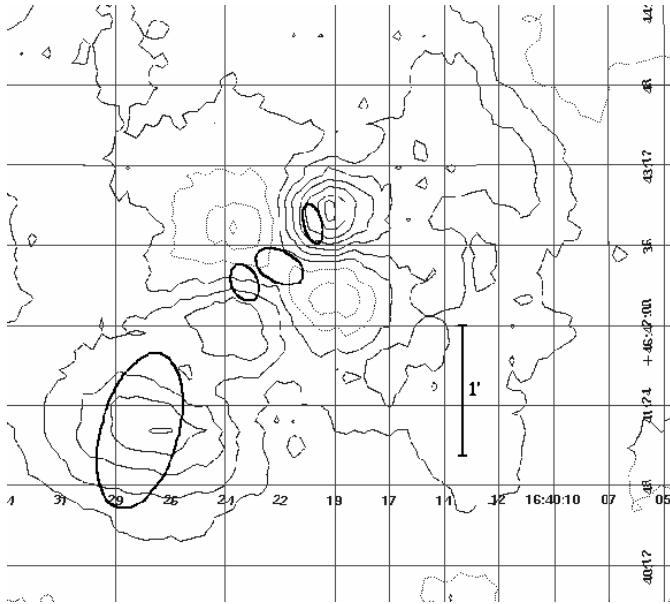


Fig. 11. Residual map of the elliptical Beta model fit (see text). Solid and dotted contour lines indicate regions with positive and negative residuals, respectively. Ellipses represent the structures detected by Wavdetect.

be obtained during a period of 1 – 2 Gyr which follows the halting of the star formation after a 1 Gyr period of constant star formation (Morris et al. 1998).

Galaxy no. 81 shows the strongest $H\delta$ EW, and it is therefore spectroscopically classified as ‘a’. However, it also shows evidence of mild [OII] emission, $EW \simeq 3 \text{ \AA}$. It would have been classified ‘e(a)’ in the scheme of Poggianti et al. (1999). The galaxy coincides with one of the X-ray peaks, identified at the smallest wavelet scale. The X-ray emission could therefore be point-like, and consistent with emission from an AGN. The lack of strong emission lines could be explained if there is substantial dust obscuration. This interpretation is consistent with the fact that e(a) galaxies are generally associated with dusty star-forming galaxies (Poggianti et al. 1999). The AGN emission should then be re-emitted in the infrared (IR). Although galaxy no. 81 was not detected at $15 \mu\text{m}$ with ISOCAM by Barvainis et al. (1999), one can see in Fig. 4 of Barvainis et al. (1999) low-level isocontours of mid-IR emission centered on this galaxy. Given that their rms noise level is $\approx 0.11 \text{ mJy}$, and their faintest detected source has a $15 \mu\text{m}$ flux density of 0.53 mJy , the $15 \mu\text{m}$ flux density of galaxy 81 should be $\lesssim 0.4\text{--}0.5 \text{ mJy}$.

Of the 5 mid-IR sources detected by Barvainis et al. (1999) in the field of A2219, three are in our spectroscopic sample. These are the galaxies no. 42, 45 and 72 (respectively no. 1, 2, and 3 in Barvainis et al.’s Table 1). Only galaxy no. 42 is a cluster member. The other two are foreground galaxies. Galaxy no. 42 is an a-type galaxy, with an $H\delta$ $EW \simeq 8 \text{ \AA}$. Its spectrum shows evidence of a mild [OII] emission, $EW \simeq 3 \text{ \AA}$. It would have been classified ‘e(a)’ in the scheme of Poggianti et al. (1999). The flux in the [OII] line can be used to compute the star formation

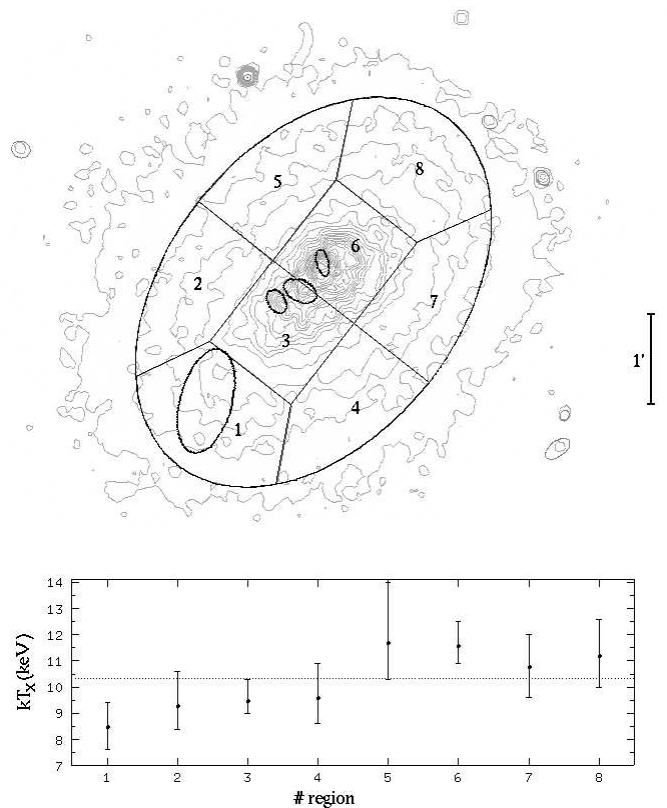


Fig. 12. Temperature map of A2219. The cluster area is divided in eight numbered sectors (top panel). Sectors are superimposed to the contour levels of the Chandra image. Ellipses show the four structures detected in the X-ray image. The graph in the bottom panel shows the temperature computed in each sector.

rate of the galaxy, using the relation of Kennicutt (1998). We find $SFR \simeq 2 \pm 1 h^{-2} M_{\odot} \text{ yr}^{-1}$.

We have examined the optical–mid-IR spectral energy distribution (SED) of galaxy no. 42, by comparing the observed data (taken from Barvainis et al. 1999) with the GRASIL models of Silva et al. (1998). The GRASIL model takes into account the effects of several kinds of dust particles on the re-processing and obscuration of the stellar radiation (see: <http://web.pd.astro.it/granato/grasil/grasil.html>). We find that the observed SED of galaxy no. 42 is best-fitted by a model of a young (3 Gyr-old) early-type spiral, with significant ongoing star formation (see Fig. 15). The best-fit model SED is used to compute the galaxy total IR luminosity, $\simeq 4 \cdot 10^{10} h^{-2} L_{\odot}$. The galaxy star formation rate, SFR, is derived from the total IR luminosity using the relation of Kennicutt (1998). We obtain $SFR \simeq 7.5 \pm 0.9 h^{-2} M_{\odot} \text{ yr}^{-1}$. This value is about 4 times higher than the estimate we obtain from the [OII] line flux. This is expected because of significant dust extinction at short wavelengths. As a matter of fact, from the best-fit model SED we estimate that dust extinction reduces the flux in the [OII] line by a factor ~ 3 .

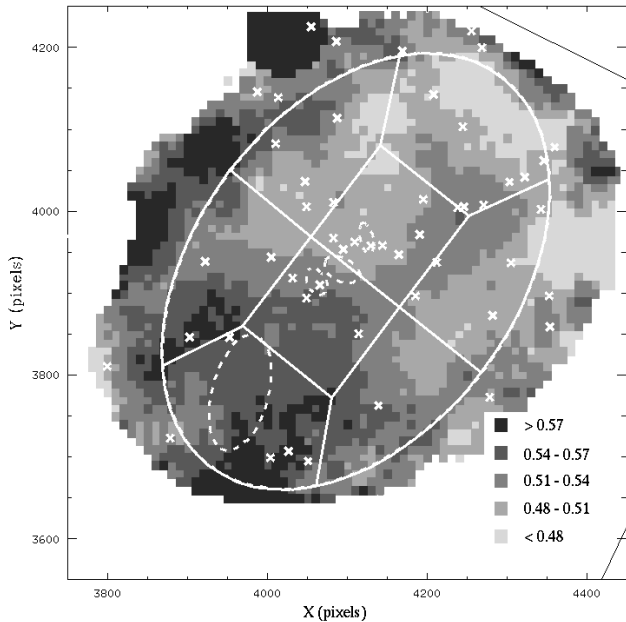


Fig. 13. Softness ratio map of A2219 (see text). Superimposed to the map are the eight sectors (see Fig. 12). Dashed ellipses are the structures detected in the X-ray image and crosses show the positions of the cluster members.

We conclude that galaxy no. 42 is a dusty star-forming galaxy, rather than a post-starburst galaxy. We thus find that both e(a) galaxies of our sample are dusty, active galaxies, a finding that supports the interpretation given by Poggianti et al. (1999) for these kind of galaxies.

With our spectral classification of a subset of A2219 galaxies, we can try to shed light on the nature of the 'blue' galaxies which are responsible for the Butcher-Oemler (BO, hereafter) effect (Butcher & Oemler 1978). We have translated the original Butcher & Oemler's definition of 'blue' galaxies to the cluster redshift and the B and R filters, by using the tables of Fukugita et al. (1995), and taking into account the Galactic absorption in the direction of A2219 (as given in the NASA Extragalactic Database). The dotted lines in Fig. 7 delimit the region of the colour-magnitude diagram where the BO galaxies are located. One can see that the BO population is of a mixed nature. First, there is a substantial amount of field galaxies, of all spectroscopic types. Among BO cluster members, the dominant population is that of a-type galaxies. As we have shown, two of these a-type galaxies are in fact dusty active galaxies, rather than pure post-starburst objects. We thus conclude that the BO population of blue galaxies in the cluster A2219 is mostly composed of galaxies having experienced a recent starburst. In some of these galaxies the star-forming activity is not over yet, although partly hidden by dust.

As for radio galaxies in the cluster, Bacchi et al. (2003) confirm the presence of three radio galaxies at the cluster

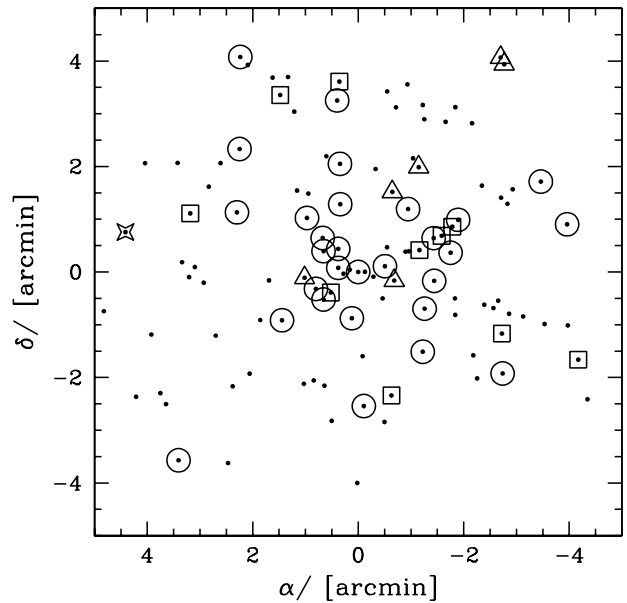


Fig. 14. Spatial distribution on the sky of 113 cluster members. Large symbols denotes spectroscopic classified galaxies: circles, triangles, squares, and stars indicate k^- , i^- , a^- , and e^- galaxies, respectively.

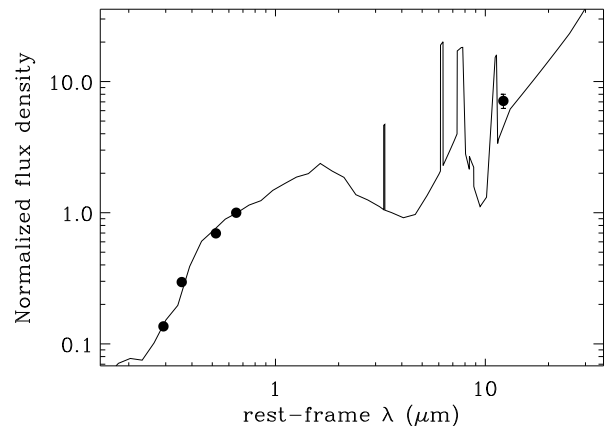


Fig. 15. Optical-mid IR spectral energy distribution of galaxy no. 42. The best-fit GRASIL model is also shown (solid line).

center of A2219 (see Owen et al. 1992) identified in our catalogue with no. 51, 77, 85 (i.e. S3, S4, and S6 respectively in Fig. 9 by Bacchi et al. 2003). The northernmost galaxy no. 77, which lies in the low-velocity tail of the cluster velocity distribution ($v = 62364 \text{ km s}^{-1}$), shows a tailed structure pointing towards NW direction, with a sharp bend towards the NE (see Owen & Ledlow 1997). The galaxy no. 85 is the second brightest galaxy of the cluster ($\sim 17 \text{ R mag}$) and lies at $< 1'$ SE separation from the cD galaxy.

6. Discussion and conclusion

We analyze the internal dynamics of A2219 on the basis of spectroscopic data for 132 galaxies in a cluster region of $\sim 5'$ ($\sim 0.8 h^{-1}$ Mpc at the cluster distance) centered on the cD galaxy. Out of 132 spectra, 27 galaxies come from new observations carried out at the TNG. We find that A2219 appears as a peak in the velocity space at $z = 0.225$, and select 113 cluster members. The investigation of the dynamical status is also performed by using X-ray data stored in the Chandra archive. Further valuable information comes from other bands – optical photometric, infrared, and radio data – which are analyzed and/or discussed, too.

The value we obtain for the line-of-sight velocity dispersion $\sigma_v \sim 1400 \text{ km s}^{-1}$ is in the high-tail of the distribution of cluster velocity dispersions (see Fadda et al. 1996; Mazure et al. 1996; Girardi & Mezzetti 2001). This global value of σ_v is consistent with the average value of $T_X \sim 10 \text{ keV}$ coming from the X-ray analysis ($\beta_{\text{spec}} = 1.10^{+0.15}_{-0.12}$, see also Fig. 4) and with the value of $L_X(0.1 - 2.4 \text{ keV}) \sim 5 h^{-2} 10^{44} \text{ erg s}^{-1}$ (Ebeling et al. 1996), converted in $L_{X,\text{bol}} \sim 2 \cdot 10^{45} h^{-2} \text{ erg s}^{-1}$ (see $L_X - \sigma_v$ relation by, e.g., Wu et al. 1999, and Girardi & Mezzetti 2001).

Therefore, on the basis of global properties only, we would conclude that A2219 is not far from the dynamical equilibrium and would trust the large virial mass estimate $M(\sim 2.2 h^{-1} \text{ Mpc}) \sim 2.8 \times 10^{15} h^{-1} M_\odot$. However, the high values of σ_v , T_X , and L_X could be due to the expected increase during a cluster-merging phase (e.g., Schindler & Böhringer 1993; Schindler & Müller 1993). Their agreement could be a mere coincidence, and our virial mass estimate an overestimate of the true value.

We find observational evidence that the cluster is not dynamically relaxed. Our optical and X-ray analyses show that A2219 is elongated in the SE–NW direction. This elongation is seen in: the spatial distribution of the colour-selected likely cluster members; the shape of the cD galaxy; the X-ray contour levels of the Chandra image; the gradient in the velocity dispersion and in the X-ray temperature. In particular the ellipticity of X-ray isophotes is significantly higher than 0 and corresponds to an axis-ratio=0.66, which is much lower than the usual value for galaxy clusters (median axis-ratio with 99% c.l. errors= $0.82^{+0.04}_{-0.02}$ from Mohr et al. 1995). Note that Dahle et al. (2002) found that the mass distribution of this cluster recovered from a weak lensing analysis appears even more elongated than the light and galaxy number density distribution.

Very interestingly, the optical data show a somewhat smaller PA than X-ray data ($\sim 110^\circ$ and $\sim 130^\circ$, respectively). A different direction in the elongation of light and hot gas distribution could be the result of a cluster merger in an advanced phase as shown by numerical simulations where collisional and collisionless components react in different way (e.g., Ricker & Sarazin 2001; Schindler 2002). In fact, the evidence of an ongoing merger in the cluster

core was first suggested by Smail et al. (1995) to explain the difference they find in the orientation of the mass and gas distributions (PA=115 and 128 degrees), as obtained from gravitational lensing analysis and ROSAT/HRI X-ray data, respectively.

As for the presence of the velocity gradient roughly in the E–W direction, this suggests that the structures are moving into the plane of the sky at $\sim 45^\circ$ (e.g., Quintana et al. 1996; Roettiger & Flores 2000). In fact, intermediate angles are the most suitable to allow detection of the cluster elongation and contemporary the velocity gradient during a merging phase.

The hypothesis of an advanced-phase merging is also supported by the lack of a cool center in the cluster (see also Allen & Fabian 1998), as expected since strong cluster mergers disrupt the cool cores (Peres et al. 1998; Roettiger et al. 1996), and the existence in the core of several star-forming or post-starburst galaxies, whose activity could be produced by the cluster merger (e.g., Bekki 1999). In particular, three of these active galaxies are part of the filament at NW of the cD, also visible as a cool component in the X-ray softness ratio map (see Fig. 8 and Fig. 13), suggesting that this structure might be already involved in a merger event. Moreover, the shape of the radio tail of the radio galaxy no. 77 indicates that the velocity of this galaxy was originally pointing towards the cluster center (cD galaxy), but has rather suddenly changed the motion direction, probably because of the cluster merger.

The structure we find in the cluster core could be related to the cluster merger, too. Considering optical data, the Dressler–Schectman test shows the possible existence of a substructure located at SE, very close to the cD galaxy. As for X-ray data, our wavelet multi-scale analysis puts in evidence three significant emission peaks located within $1'$ from the cluster center. Of these, two peaks are possibly connected to intrinsic X-ray emission from the cD and the active galaxy no. 81, but no optical counterpart is found for the third, intermediate peak. Our wavelet X-ray analysis also detects an external diffuse substructure located $2'$ SE of the cD galaxy. We suggest that this structure is a premerging clump. In fact, it coincides with the cold SE X-ray region and thus could be well explained by the two-dimensional superposition of a cold clump in the foreground of the main cluster. The presence of this foreground clump could also explain why, on average, the velocity at the East is lower than in the West since at least for some galaxies the low velocity is of cosmological rather than of kinematic origin. These anomalous low velocity galaxies could also produce a spurious enhancement of the observed velocity dispersion in the SE region (see Table 2). A population of very close foreground galaxies could also explain why *very red* galaxies strangely differ from *not-very red* galaxies both in kinematic and spatial properties (see Sect. 3.3). In fact, while the former are really associated with the main structure of A2219, the latter could be mixed with the clump members, i.e. a population of foreground – and thus less red – galaxies. Unfortunately,

we have very poor redshift information in the SE region to confirm our hypothesis and identify clump members.

On a much larger scale, the cluster is not so well isolated in the redshift space, and a next possible merging clump might be the one at $z \sim 0.19$ (see Fig. 2).

Summarizing the above evidence, we suggest a complex merging scenario for A2219 involving many clumps, possibly in different dynamical states. We suggest that the main, original structure (hosting the cD galaxy) is subject to an ongoing merger with few clumps aligned in a foreground filament obliquely oriented with respect to the line-of-sight; the filament projected on the sky lies in the SE–NW direction. In this scenario, the merging with one or more clumps are already in a very advanced phase, well after the first core passage, while one or more clumps are still in a pre-merging phase.

In the context of the above scenario, we argue that the presence of a radio-halo in A2219 is related to the existence of an ongoing, very advanced phase of merging between the main cluster and one or more groups. In fact, the elongation of radio map contours (see Fig. 10) has the same direction of the X-ray surface brightness contours. Moreover, the time necessary to re-accelerate the electrons producing the radio-halo as a consequence of the cluster merger (~ 1 Gyr) is comparable to that needed to obtain post-starburst spectral signatures in galaxies of which A2219 is rich (see Sect. 5).

In conclusion, our scenario supports the view of the connection between extended radio emission and merging phenomena in galaxy clusters.

Acknowledgements. We thank Luca di Fabrizio for B and R calibration observations at the TNG telescope and the anonymous referee for useful suggestions and comments. We particularly thank Ian Smail for providing us accurate Palomar 5-m telescope photometry. Work partially supported by the Italian Ministry of Education, University, and Research (MIUR, grant COFIN2001028932 "Clusters and groups of galaxies, the interplay of dark and baryonic matter"), by the Italian Space Agency (ASI), and by INAF (Istituto Nazionale di Astrofisica) through grant D4/03/IS. This publication makes use of data accessed as Guest User at the Canadian Astronomy Data Center, which is operated by the Dominion Astrophysical Observatory for the National Research Council of Canada's Herzberg Institute of Astrophysics (<http://cadwww.dao.nrc.ca/cfht/cfht.html>), as well as of data obtained from the Chandra data archive at the NASA Chandra X-ray center (<http://asc.harvard.edu/cda/>).

References

- Abell, G.O., Corwin, H.G. Jr., & Olowin, R.P. 1989, *ApJS*, 70, 1
- Allen, S.W., Edge, A.C., Fabian, A.C., et al. 1992, *MNRAS*, 259, 67
- Allen, S.W., & Fabian, A.C. 1998, *MNRAS*, 297, L57
- Allen, S.W. 2000, *MNRAS*, 315, 269
- Bacchi, M., Feretti, L., Giovannini, G., & Govoni, F. 2003, *A&A*, 400, 465
- Balogh, M.L., Morris, S.L., Yee, H.K.C., Carlberg, R.G., & Ellingson, E. 1999, *ApJ*, 527, 54
- Bardelli, S., Zucca, E., Vettolani, G., et al. 1994, *MNRAS*, 267, 665
- Barena, R., Biviano, A., Ramella, M., Falco, E.E., & Seitz, S. 2002, *A&A*, 386, 816
- Barvainis, R., Antonucci, R., & Helou, G. 1999, *AJ*, 118, 645
- Beers, T.C., Flynn, K., & Gebhardt, K. 1990, *AJ*, 100, 32
- Beers, T.C., Forman, W., Huchra, J.P., Jones, C., & Gebhardt, K. 1991, *AJ*, 102, 1581
- Bekki, K. 1999, *ApJ*, 510, L15
- Bertin, E., & Arnouts, S. 1996, *A&AS*, 117, 393
- Böhringer, H., & Schuecker, P. 2002, in "Merging Processes in Galaxy Clusters", eds. L. Feretti, I.M. Gioia, & G. Giovannini, Kluwer Ac. Pub., The Netherlands, in press: Observational signatures and statistics of galaxy cluster mergers
- Buote, D.A. 2002, in "Merging Processes in Galaxy Clusters", eds. L. Feretti, I.M. Gioia, & G. Giovannini, Kluwer Ac. Pub., The Netherlands, in press: Optical Analysis of Cluster Mergers
- Butcher, H., & Oemler, A., Jr. 1978, *ApJ*, 219, 18
- Carlberg, R.G., Yee, H.K.C., Ellingson, E., et al. 1997, *ApJ*, 476, L7
- Colless, M., & Dunn, A.M. 1996, *ApJ*, 458, 435
- Couch, W.J., Ellis, R.S., Sharples, R.M., & Smail, I. 1994, *ApJ*, 430, 121
- Dahle, H., Kaiser, N., Irgens, R.J., Lilje, P.B., & Maddox, S. J. 2002, *ApJS*, 139, 313
- Danese, L., De Zotti, C., & di Tullio, G. 1980, *A&A*, 82, 322
- den Hartog, R., & Katgert, P. 1996, *MNRAS*, 279, 349
- Dickey, J.M., & Lockman, F.J. 1990, *ARA&A*, 28, 215
- Dressler, A., & Shectman, S.A. 1988, *AJ*, 95, 985
- Dressler, A., Smail, I., Poggianti, B.M., et al. 1999, *ApJS*, 122, 51
- Ebeling, H., Voges, W., Böhringer, H., et al. 1996, *MNRAS*, 281, 799
- Ellingson, E., & Yee, H.K.C. 1994, *ApJS*, 92, 33
- Ensslin, T.A. 2000, in "Cluster Mergers and their Connection to Radio Sources", 24th meeting of the IAU, Joint Discussion 10, August 2000, Manchester, England.
- Ensslin, T.A., & Röttgering, H. 2002, *A&A*, 396, 83
- Evrard, A.E. & Gioia, I.M. 2002, in "Merging Processes in Galaxy Clusters", eds. L. Feretti, I.M. Gioia, & G. Giovannini, Kluwer Ac. Pub., The Netherlands: Clusters, Cosmology and Mergers
- Fadda, D., Girardi, M., Giuricin, G., Mardirossian, F., & Mezzetti, M. 1996, *ApJ*, 473, 670
- Fasano, G., & Franceschini, A. 1987, *MNRAS*, 225, 155
- Feretti, L., & Giovannini, G. 1996, "Extragalactic radio sources", proceedings of the 175th Symposium of the International Astronomical Union, held in Bologna, Italy, 10-14 October 1995. Edited by Ron D. Ekers, C. Fanti, and L. Padrielli. Published by Kluwer Academic Publishers, p. 333.
- Feretti, L. 1999, MPE Report No. 271
- Feretti, L. 2002, "The Universe at Low Radio Frequencies", Proceedings of IAU Symposium 199, held 30 Nov - 4 Dec 1999, Pune, India. Edited by A. Pramesh Rao, G. Swarup, and Gopal-Krishna, 2002., p.133
- Fukugita, M., Shimasaku, K., & Ichikawa, T. 1995, *PASP*, 107, 945
- Gebhardt, K., & Beers, T.C. 1991, *ApJ*, 383, 72
- Giovannini, G., Tordi, M., & Feretti, L. 1999, *New Astronomy*, 4, 141

- Giovannini, G., & Feretti, L. 2002, in “Merging Processes in Galaxy Clusters”, eds. L. Feretti, I.M. Gioia, & G. Giovannini, Kluwer Ac. Pub., The Netherlands: Diffuse Radio Sources and Cluster Mergers
- Girardi, M., Fadda, D., Giuricin, G. et al. 1996, *ApJ*, 457, 61
- Girardi, M., Giuricin, G., Mardirossian, F., Mezzetti, M., & Boschin, W. 1998, *ApJ*, 505, 74
- Girardi, M., & Mezzetti, M. 2001, *ApJ*, 548, 79
- Girardi, M., & Biviano, A. 2002, in “Merging Processes in Galaxy Clusters”, eds. L. Feretti, I.M. Gioia, & G. Giovannini, Kluwer Ac. Pub., The Netherlands: Optical Analysis of Cluster Mergers
- Gómez, P.L., Hughes, J.P., & Birkinshaw, M. 2000, *ApJ*, 540, 726
- Govoni, F., Feretti, L.; Giovannini, G., et al. 2001, *A&A*, 376, 803
- Hammer, F., Flores, H., Lilly, S.J., et al. 1997, *ApJ*, 481, 49
- Kennicutt, R.C. 1992, *ApJS*, 79, 225
- Kennicutt, R.C. 1998, *ARA&A*, 36, 189K
- Malamuth, E.M., Kriss, G.A., Dixon, W. Van Dyke, Ferguson, H.C., & Ritchie, C. 1992, *AJ*, 104, 495
- Mazure, A., Katgert, P., den Hartog, P., et al. 1996, *A&A*, 310, 31
- Mercurio, A., Girardi, M., Boschin, W., Merluzzi, P., & Busarello, G. 2003, *A&A*, 397, 431
- Mohr, J.J., Evrard, A.E., Fabricant, D.G., & Geller, M.J. 1995, *ApJ*, 447, 7
- Morris, S.L., Hutchings, J.B., Carlberg, R.G., et al. 1998, *ApJ*, 507, 84
- Owen, F.N., White, R.A., & Burns, J.O. 1992, *ApJS*, 80, 501
- Owen, F.N., & Ledlow, M.J. 1997, *ApJS*, 108, 410
- Peres, C.B., Fabian, A.C., Edge, A.C., et al. 1998, *MNRAS*, 298, 416
- Pisani, A. 1993, *MNRAS*, 265, 706
- Pisani, A. 1996, *MNRAS*, 278, 697
- Poggianti, B.M., Smail, I., Dressler, A., et al. 1999, *ApJ*, 518, 576
- Postman, M., Lubin, L.M., & Oke, J.B. 1998, *AJ*, 116, 560
- Press, W.H., Teukolsky, S.A., Vetterling, W.T., & Flannery, B.P. 1992, in “Numerical Recipes” (Second Edition), (Cambridge University Press)
- Quintana, H., Carrasco, E.R., & Reisenegger, A. 2000 *AJ*, 120, 511
- Quintana, H., Ramirez, A., & Way, M.J. 1996, *AJ*, 112, 36
- Raymond, J.C., & Smith, B.W. 1977, *ApJS*, 35, 419
- Ricker, P.M., & Sarazin, C.L. 2001, *ApJ*, 561, 621
- Rizza, E., Burns, J.O., Ledlow, M.J., et al. 1998, *MNRAS*, 301, 328
- Roettiger, K., Burns, J.O., & Loken, C. 1996, *ApJ*, 473, 651
- Roettiger, K., Loken, C., & Burns, J.O. 1997, *ApJS*, 109, 307
- Roettiger, K., & Flores, R. 2000, *ApJ*, 538, 92
- Sarazin, C.L. 2002, in “Merging Processes in Galaxy Clusters”, eds. L. Feretti, I.M. Gioia, & G. Giovannini, Kluwer Ac. Pub., The Netherlands: The Physics of Cluster Mergers
- Schindler, S., & Böhringer, H. 1993, *A&A*, 269, 83
- Schindler, S., & Müller, E. 1993, *A&A*, 272, 137
- Schindler, S. 2002, in “Merging Processes in Galaxy Clusters”, eds. L. Feretti, I.M. Gioia, & G. Giovannini, Kluwer Ac. Pub., The Netherlands: Mergers of Galaxy Clusters in Numerical Simulations
- Schuecker, P., Böhringer, H., Reiprich, T.H., & Feretti, L. 2001, *A&A*, 378, 408
- Silva, L., Granato, G.L., Bressan, A., & Danese, L. 1998, *ApJ*, 509, 103
- Smail, I., Hogg, D.W., Blandford, R., et al. 1995, *MNRAS*, 277, 1
- Smail, I., Edge, A.C., Ellis, R.S., & Blandford, R.D. 1998, *MNRAS*, 293, 124
- Terlevich, A.I., Kuntschner, H., Bower, R.G., Caldwell, N., & Sharples, R.M., *MNRAS*, 310, 445
- Tonry, J., & Davis, M. 1979, *ApJ*, 1511
- White, D.A. 2000, *MNRAS*, 312, 663
- White, S.D.M. 1997, in “The Evolution of the Universe”, report of the Dahlem Workshop on the Evolution of the Universe, Berlin, September 10-15, 1995. Edited by G. Borner and S. Gottlober. New York : J. Wiley, 1997., p.227
- Wu, X.-P., Xue, Y.-J., & Fang, L.-Z. 1999, *ApJ*, 524, 22